Applied Catalysis B: Environmental 252 (2019) 77–85

Contents lists available at ScienceDirect

Applied Catalysis B: Environmental

journal homepage: www.elsevier.com/locate/apcatb

Enhanced photocatalytic activity of Pt-TiO_2/WO_3 hybrid material with energy storage ability

Hayat Khan, Marco G. Rigamonti, Daria C. Boffito*

Polytechnique Montréal, Dept. of Chemical Engineering, 2900 Boul. Édouard-Montpetit, 2500 Chemin Polytechnique, Montréal, QC, H3T 1J4, Canada

ARTICLE INFO

Keywords:
Pt photocatalyst
TiO_2-WO_3 photocatalyst
Mixed oxides
Energy storage
Apparent band gap
Activity in the dark

ABSTRACT

We aimed at producing a photocatalyst having UV–vis activity with residual energy storage ability in absence of irradiation. We synthesized a series of catalysts with Pt supported over mixed titanium-tungsten oxides (TiO_2/WO_3). The methods were spray dried assisted sol-gel and crash precipitation. TiO_2 maintained its tetragonal anatase phase and WO_3 its monoclinic structure. The hybrid samples (Pt_xTW, where x = 0–1.2 wt.%) have significantly higher BET surface area (204.0 - 283.0 m^2/g) compared to control $Pt_{0.8}$T (265.0 m^2/g) and $Pt_{0.8}$W (54.5 m^2/g) samples. XPS analysis detected the presence of metallic platinum (Pt°), which actively takes part in the enhanced photons absorption of the photocatalyst, as depicted from UV–vis-DRS study. The $Pt_{0.8}$TW- optimum Pt loading- is characterized by a visible absorption edge at 501.0 nm compared to the control $Pt_{0.8}$T (444.0 nm) and $Pt_{0.8}$W (540.5 nm). Microscopy images showed homogenous and uniform distribution of the oxides, and Pt particles and the FTIR analyses evidenced greater adsorption of OH^- groups on the hybrid samples surface. In the activity tests, the $Pt_{0.8}$TW outperforms the other samples in the aqueous degradation of the model pollutant methylene blue (MB) (78.0% and 56.0% in UV and visible light), with an additional hour of energy storage ability in absence of irradiation, then reaching a final degradation of 98.0% and 77.0% under UV and Visible light, respectively. In connection to the activity tests, scavenging experiments revealed that hydrogen peroxide (H_2O_2) and hydroxyl radicals ($OH^•$) were the main species responsible for the pollutant degradation.

1. Introduction

Research on photocatalysis from the last two decades concluded that titanium dioxide (TiO_2) is arguably the most promising material for applications to air and water purification from recalcitrant organic and inorganic pollutants [1–4]. Bare TiO_2 is active only under ultraviolet (UV) light because of the size of its bandgap (E_g TiO_2 ~ 3.0–3.2 eV). Moreover, the fast recombination of the photocatalytically generated charge carriers competes with the electron transfer of the reactants adsorbed on the catalyst surface, which makes TiO_2 photocatalysis inherently inefficient [1,5]. This has prompted scientists to search for strategies to increase TiO_2 UV and visible light activity, and energy storage ability to design photocatalysts with residual activity in the dark. New photocatalyst designs should then address these main drawbacks, which limit the large-scale application of TiO_2 [6–8]. Coupling TiO_2 with a metal oxide or a metal that absorbs visible light and possessing a conduction band (CB) at a lower energy level, and CB and a valance band (VB) with higher or equal energy compared to TiO_2 increases the separation of the charge carriers [9,10]. The photoexcited electrons may diffuse from TiO_2 CB to that of the other species, while photogenerated holes remain either trapped within the TiO_2 particles, or are transferred back from the coupled metal oxide to TiO_2 VB. Among semiconductor oxides, crystalline tungsten oxide (WO_3) has some advantages including: induction of surface acidity to promote adsorption of OH^-; water and pollutant molecules [11,12]; energy storage ability; visible light photosensitivity (E_g = 2.6 eV) [13]; energy levels enabling the electrons photogenerated in TiO_2 CB to transfer into the WO_3 CB, and likewise the photopromoted holes in WO_3 CB to diffuse into the VB of TiO_2 [5,14].

Riboni et al. [15] prepared WO_3-TiO_2 mixed oxide by a sol-gel method. The photocatalyst with the optimum tungsten content of 3% had higher activity than TiO_2 P25 and degraded 31% acetaldehyde in 2 h in the gas phase under mainly visible irradiation. Baia et al. [16] synthesized a TiO_2/WO_3 composite by adding TiO_2 and WO_3 powder to distilled water with a pH equal to the average of IEP (isoelectric point) of TiO_2 and WO_3 and dried the resulting suspension to a final TiO_2/WO_3 ratio of 76:24. The photocatalysts were 10% more active in the degradation of methyl orange under UV light compared to TiO_2 P25. Pandi and Gopinathan [17] produced TiO_2/NiO and TiO_2/WO_3 nanocomposites by hydrothermal synthesis and surface modification

* Corresponding author.
E-mail address: daria-camilla.boffito@polymtl.ca (D.C. Boffito).

https://doi.org/10.1016/j.apcatb.2019.04.019
Received 17 November 2018; Received in revised form 26 March 2019; Accepted 8 April 2019
Available online 10 April 2019
0926-3373/ © 2019 Elsevier B.V. All rights reserved.

(mixing TiO_2 with either WO_3 or NiO powder in the presence of chloroform). The increased degradation of aqueous eosin-Y with TiO_2/WO_3 was due to visible light absorption and reduced carrier recombination rate. Ramos-Delgado et al. [11] prepared TiO_2 modified with WO_3 (2 wt. %) by sol-gel method and degraded malathion (pesticide) under solar irradiation, The TiO_2/WO_3 completely degraded malathion in 120 min. Its higher activity was ascribed to the reduced charge recombination and higher surface area. Dozzi et al. [5] synthesized TiO_2/WO_3 systems by incipient wetness with a W/T molar ratio ranging from 0.2 to 5. They found that WO_3 promoted the formation of smaller TiO_2 particles during annealing, thus resulting in a higher surface area. Akurati et al. [18] synthesized flame-made WO_3/TiO_2 powders with marginally higher activity in the degradation of methylene blue compared to TiO_2 P25. The WO_3/TiO_2 samples had higher surface acidity and better charge separation due to the coupling effect. Cao et al. [19] obtained TiO_2/WO_3 composite by wet chemical method by mixing Degussa P25 with tungstic acid. The photocatalyst exhibited energy storage ability in the course of electrochemical measurements. We recently prepared a series of TiO_2/WO_3 (TW_x)with WO_3 content (x) varying from 0.025 to 0.1, whereby the one at 0.075 was the most active accounting for the highest SSA (221 m^2 g^{-1}) and highest concentration of [001] anatase planes. $TW_{0.075}$ degraded over 80% methylene blue in 70 min under UV irradiation, and additional 10% once the irradiation was off until 100 min, indicating electron storage ability [20].

To enhance further the electron storage ability, visible activity and electron-hole separation, Pt creates Schottky-type junctions, thus facilitating the charge transfer at the catalyst/environment interface [21–23]. In such a context, Spanu et al. [1] synthesized hexagonally-ordered anodic TiO_2 nanotube layers on the top of which W and Pt were sputtered in sequence, whereby WO_3 was thermally formed in a layer if few nm. The photocatalyst with 5 nm of WO_3 at the top lead to the highest H_2 evolution from H_2O splitting, i.e. 5.2 μL h^{-1} cm^{-2}. Abe et al. [24] observed acetaldehyde degradation under visible light over Pt-WO_3 one order of magnitude higher compared to Pt and N-doped TiO_2. The WO_3 CB electrons move to Pt particles accelerating the multi-electron reduction mechanism. Qamar et al. [25] attributed the increased sunlight photocatalytic activity of Pt-WO_3 to uniformly dispersed Pt particles with narrow size distribution (2–4 nm). Ohashi et al. [26] used the complex polyelectrolyte-mediated electrostatic adsorption approach to prepare Pt-WO_3 combined with TiO_2. This sample completely degraded acetone on the gas phase in 400 min under visible light, vs. 700 min due suppressed electron-hole recombination compared to the Pt/WO_3 sample.

We hereby report for the first time the facile spray-dry assisted sol-gel synthesis of UV–vis macroporous Pt loaded onto TiO_2/WO_3 composite material. The originality of the current work encompasses: (i) The uniform deposition of Pt on the TiO_2/WO_3 semiconductor prepared through a facile sol-gel and crash precipitation methods followed by spraying drying and calcination at 600 °C. (ii) The synthesis of well crystalline Pt- TiO_2/WO_3 with very high surface area (204–283 m^2/g) and porosity, while maintaining macroporosity at the same time. (iii) The variation of the Pt amount from 0.2 to 1.2 wt. %, and finally (iii) We propose a mechanism to illustrate the transfer pathways of the photopromoted electron-hole pairs towards the increased photocatalytic activity for the degradation of the model pollutant methylene blue. We also show the electron storage ability mechanism for the residual activity in the dark. Characterization details of the Pt-TiO_2/WO_3 powders include XRD, FTIR, electron microscope imaging, N_2 physisorption, UV–vis-DRS, Raman, photoluminescence (PL) and XPS spectroscopy.

2. Materials and Methods

2.1. Chemicals

Titanium butoxide ($Ti(oBu)_4$, purum ≥ 97.0% gravimetric), ammonium paratungstate hydrate (99.99% trace metal basis, gravimetric), formic acid (reagent grade ≥ 95%) and Chloroplatinic acid hydrate, (≥ 99% trace metal basis) were supplied by Sigma Aldrich, Canada. Hydrochloric acid (certified ACS plus) was supplied by Fischer Scientific. Commercial Alcohols (Boucherville, Quebec, Canada) provided the anhydrous ethyl alcohol. All the chemicals were used as received without any further purification. Laboratory deionized water was used throughout this work.

2.2. Catalyst preparation

Traditional sol-gel method was used for the synthesis of TiO_2. Titanium butoxide, anhydrous ethyl alcohol, formic acid and water were mixed in the molar ratio of 60:500:27:1500 for one hour at room temperature. A pre-established amount of titanium precursor was added to anhydrous ethyl alcohol under vigorous stirring, followed by the drop-wise addition of water and formic acid. A milky sol of titanium hydroxide instantaneously formed sue to hydrolysis and condensation reactions in the reacting mixture.

We simultaneously prepared WO_3 by a crash precipitation technique. Ammonium paratungstate ($(NH_4)_{10}H_2(W_2O_7)_6$), hydrochloric acid (HCl) and water were used in the molar ratio of 0.005:200:500. Ammonium paratungstate dissolved in HCl under stirring followed by rapid addition of this solution to water, resulting in the crash precipitation of a yellow white precipitate of WO_3. The precipitate was washed several times with deionized water (8 x 100 mL). Finally, 20 mL of deionized water were added to the precipitate under constant stirring to obtain the WO_3 suspension.

In the next steps, we added the WO_3 suspension to the stable sol of titanium hydroxide and stirred the hybrid suspension for 3 h before spray drying it. We followed the experimental protocol stated elsewhere [20], as well as the same equipment (Yamato GB-22 dryer) to produce the final TiO_2/WO_3 powders. In the final step the dried powders were calcined at a temperature of 600 °C in a muffle furnace for 2 h to produce the crystalline hybrid TiO_2/WO_3 material.

We synthesized the control Pt-TiO_2 and Pt-WO_3 powders following the same procedure as for TiO_2 and WO_3, except dissolving the Pt precursor in water before adding it to the solution of titanium butoxide and anhydrous ethyl alcohol (in TiO_2 synthesis) and to WO_3 precipitate (in WO_3 synthesis). It should be noted that formic acid in the synthesis process also acts as a reducing agent for Pt precursor. In the synthesis of hybrid powders we added Pt-WO_3 suspension to the stable sol of TiO_2 before spray drying it. The Pt precursor concentration was calculated basing on a Pt weight percentage of 0, 0.2, 0.4, 0.6, 0.8, 1.0 and 1.2%. The final material was denoted as to Pt_xT, Pt_xW and Pt_xWT, where x is the Pt content (wt.%).

In all the hybrid samples the molar ratio TiO_2:WO_3 is 1:1.

2.3. Characterization techniques

A Phillips X'PERT diffractometer with monochromatic high intensity Cu-kα radiation (λ = 1.54178 Å) recorded the X-ray diffraction (XRD). The scanning range was 2θ = 10 - 80°, and the operating conditions were 30 kV and 40 mA.

Fourier transform infrared (FTIR) spectra of the samples mixed with potassium bromide (KBr, as a reference) were obtained on a Bruker Tensor 27 with OPUS data collection program (V 1.1) in the energy range of 5000–400 cm^{-1}.

Field emission scanning electron microscope (FESEM-JEOL JSM-7600 F) operated at a voltage of 10 kV with an energy range of 10 keV and Transmission electron microscope (Phillips Technai G2 20TEM

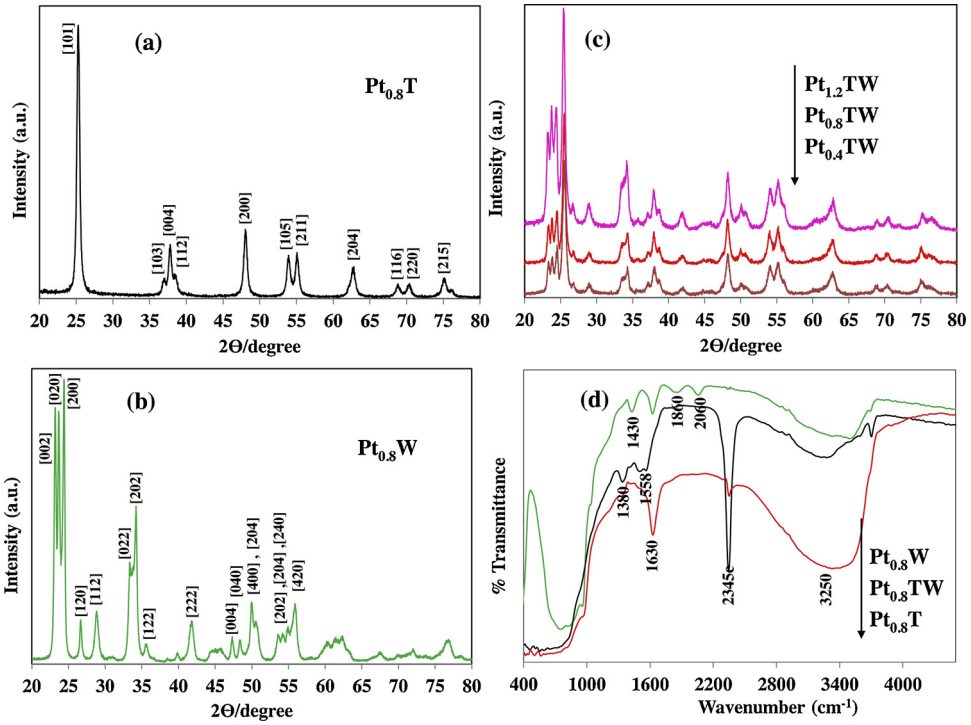

Fig. 1. XRD spectra of (a) $Pt_{0.8}T$, (b) $Pt_{0.8}W$ and (c) Pt_xTW samples, (d) FTIR spectra, all the samples were calcined at 600 °C, respectively.

(FET, US)) operated at 200 kV were used to generate images of the powders at several magnifications. FESEM equipped with an energy dispersive X-ray (EDX) detector was used to confirm the deposited Pt in the prepared catalyst powders.

A Quantachrome Autosorb-1 Instrument determined the textural properties of the photocatalysts by measuring the N_2 adsorption and desorption isotherms at 77 K, after degassing the sample under vacuum at 200 °C for 20 h. The specific surface area was calculated with the BET (Brunauer-Emmett-Teller) method (P/P_0: 0.05-0.30, C constant: 50–200). The BJH (Barrett-Joyner-Hallender) theory was considered to measure the mesopore size distribution (desorption branch, P/P_0: 0.15-0.995). The characteristic pore size for the microporous samples (DeBoer thickness) were calculated following the V-t method.

A Thermo Scientific UV–vis Evolution 300 spectrophotometer equipped with an integrated Pike technologies EasiDiff measured the diffuse reflectance spectra (DRS) in the 190–900 nm range with potassium bromide (KBr) as a reference.

A Renishaw InVia Reflex Raman microscope with an excitation laser wavelength of 514 nm, laser power of 300 mW and exposure time of 10 s at RT recorded the spectra of the powders.

A Perkin-Elmer LS-55 fluorescence spectrometer recorded photoluminescence (PL) spectra at an excitation wavelength of 320 nm of a Xe lamp. A 390 nm cut-off filter precluded the scattered Xe light.

X-ray photoelectron spectroscopy (VG ESCALAB 3 Mark II) equipped with X-ray source of Al Kα (1486.6 eV) at a base pressure below 10^{-9} Torr was used to evaluate the oxidation state of the elements. All the elements present in the powder were identified first in the measured survey spectrum, followed by a high-resolution spectrum of the known elements at a pass energy of 20 eV and 0.05 eV steps. The XPS data was processed on a VG Avantage software, all peaks were calibrated by setting the major C1s peak to 285.0 eV, attributed to adventitious carbon.

The hydroxyl radicals ($OH^{\bullet}$) concentration on the surface of the synthesized powders in water under illumination was measured by a terephthalic acid (TA) fluorescence probe technique [27]. A FluroMax-2 spectrofluorometer equipped with a Xe lamp measured the PL spectra of the produced 2-hydroxyterephthalic acid (TAOH).

Inductively coupled plasma–mass spectrometry (ICP–MS, PerkinElmer/Sciex ELAN Dynamic Reaction Cell (DRCPlus) coupled with a PerkinElmer AS-93plus Autosampler with Elan v. 3.3 software for data collection) evaluated the stability of the Pt_xWT powders by recording the at. % of the Ti, W and Pt elements in the photocatalytic solution.

2.4. Photocatalytic activity

We measured the photocatalytic activity of the samples against the photodegradation of methylene blue (MB) dye as a model pollutant at room temperature. An ultrasound bath sonicated the mixtures of the photocatalyst (0.2 g L^{-1}) and MB (6.0 mg L^{-1}) in separate flasks to reduce particles agglomeration. We added both the photocatalyst suspension and MB solution to a batch reactor, and deionized water made up the final volume to 1.5 L. Stirring the reactor suspension for 30 min ensured the establishment of the adsorption/desorption equilibrium before light irradiation. A single UV light source (GPH212T5L/4, λ_{max} = 254 nm - Germicidal UVC lamp, Atlantic Ultraviolet Corp., Maximum incident photon flux per unit volume at the mid section of the reactor was approximately 1.3×10^{-3} Einstein min^{-1} L^{-1} [28]) protected in a quartz sleeve was vertically placed at the center point inside the batch reactor. To supply oxygen in the bulk, filtered air bubbled continuously throughout the experiment. Each experiment lasted 30 min under UV irradiation. We withdrew sample aliquots at regular intervals of 10 min. We filtered all samples (Millipore filters, porosity 0.22 µm) to remove possible catalyst particles prior to analysis. A UV–vis spectrophotometer followed the photocatalytic decomposition of MB by measuring at 664 nm the maximum absorbance of MB solution. A Fisher Accumet TMAB15 pH meter equipped with a glass pH electrode recorded the *pH* throughout the experiments: the *pH* was constant at 5.5–5.65 in all the activity experiments.

In the visible photocatalytic experiments, light with λ_{range} output at 420–660 nm (irradiance = 270 W/m^2) irradiated the 0.8 L reactor solution (0.1 g L^{-1} of photocatalyst powder and 0.035 g L^{-1} of MB) for 30 min. The lamp inserted vertically in the quartz sleeve was a mercury lamp (180 W Hg-medium pressure lamp, Heraeus Nobel Light,

Table 1
Crystallite size, BET surface area and BJH pore distribution and band gap energy values of the as-synthesized samples calcined at 600 °C.

Sample	Crystallite size* (nm)		BET surface area* (m^2/g)	Porosity (%)		Band gap (eV)†
				micro	meso-macro	
$Pt_{0.8}T$	18.0		265	29.0	13.0	2.80
$Pt_{0.8}W$		27.5	54.5	1.4	73.0	2.30
$Pt_{0.2}TW$	16.0	18.0	204	23.0	22.0	2.90
$Pt_{0.4}TW$	18.0	25.0	208	23.0	21.0	2.84
$Pt_{0.6}TW$	18.0	24.5	245	25.0	35.0	2.72
$Pt_{0.8}TW$	13.0	18.0	283	30.0	36.0	2.48
$Pt_{1.0}TW$	15.6	22.5	217	23.0	26.0	2.45
$Pt_{1.2}TW$	19.5	21.5	214	24.0	12.0	2.52

* the uncertainty in crystallite size is < 1.2 nm, while in the surface area is < 0.5 m^2/g.
† the uncertainty in bandgap is < 0.3 eV.

Germany). We used a UV blocking film (UVPS, USA) to eliminate any UV light contribution. Cold water circulated in the outer jacked of the reactor to maintain the reactor solution temperature at 25–30 °C. We followed the same analytical procedure to determine the MB degradation as in the UV photocatalytic experiments.

3. Results and discussion

3.1. Catalyst characterization

The XRD profiles (Fig. 1(a–b)) shows that the control $Pt_{0.8}T$ and $Pt_{0.8}W$ powders are composed of pure anatase TiO_2 (JCPDS No: 21-1272) and monoclinic WO_3 (JCPDS No: 43-1053) structure respectively, while the composite Pt_xTW powders (Fig. 1c) exhibit of both the semiconductors oxides (TiO_2/WO_3) peaks with variable intensities. The XRD peaks reflections are very intense, indicating the well crystalline nature of all the powders. Moreover, we did not observe any peak belonging to Pt, ascribable to the uniform distribution of Pt on the mixed oxides. The major peaks including [101] at 2Θ = 25.2° of TiO_2 and [200] at 2Θ = 24.2° of WO_3 were taken into account to calculate the crystallite sizes shown by the Scherrer approximation (Table 1) [20]. Compared to control samples, the crystallite sizes in hybrid powders (Pt_xTW) are in general smaller. The particle size of hybrid samples has a minimum corresponding to a Pt content of 0.8 wt.%. For Pt loadings > 0.8 wt.%, the crystallite size of TiO_2 (T) and WO_3 (W) increases promoting the agglomeration of precipitated particles, while supressing the nucleation and growth of the particles, as the decreased intensity of the major peaks illustrate.

Fig. 1(d) illustrate the FTIR spectra of selected powders. In the sample $Pt_{0.8}T$ the peaks at 1380 and 1558 cm^{-1} correspond to symmetric $\upsilon(COO)_s$ and asymmetric $\upsilon(COO)_{as}$ carboxylate stretches due to the use of formic acid in the sol-gel peptization step [29]. The small peaks in the range 450–900 cm^{-1} correspond to Ti−O−Ti and Ti−O stretches. In the sample $Pt_{0.8}W$, the broad absorption peaks in the range 600–1000 cm^{-1} are characteristic of the different O−W−O stretching vibrations, while the four peaks at 1433, 1623, 1860 and 2060 cm^{-1} belongs to [OH, W−O] [30], OH bending mode of adsorbed water, and combination modes of the W−O bonds in the oxide lattice, respectively. Compared to the control samples, in the hybrid sample $Pt_{0.8}TW$ the very broad and deep trough in the range 3200–3600 cm^{-1} peaking at 3400 cm^{-1} relates to OH^- groups, while the peak at 1630 cm^{-1} corresponds to the bending mode of coordinated water. This clearly illustrates that the hybrid powder is more susceptible to generate $OH^{\cdot}$ radicals in the photocatalytic process due to the presence of absorbed water and OH groups on the surface. It is also noteworthy that in $Pt_{0.8}T$ powders, the very intense peak at 2345 cm^{-1} is unexpected and ascribed to atmospheric CO_2 adsorption, indicating that Pt-TiO_2 was contaminated by the atmosphere.

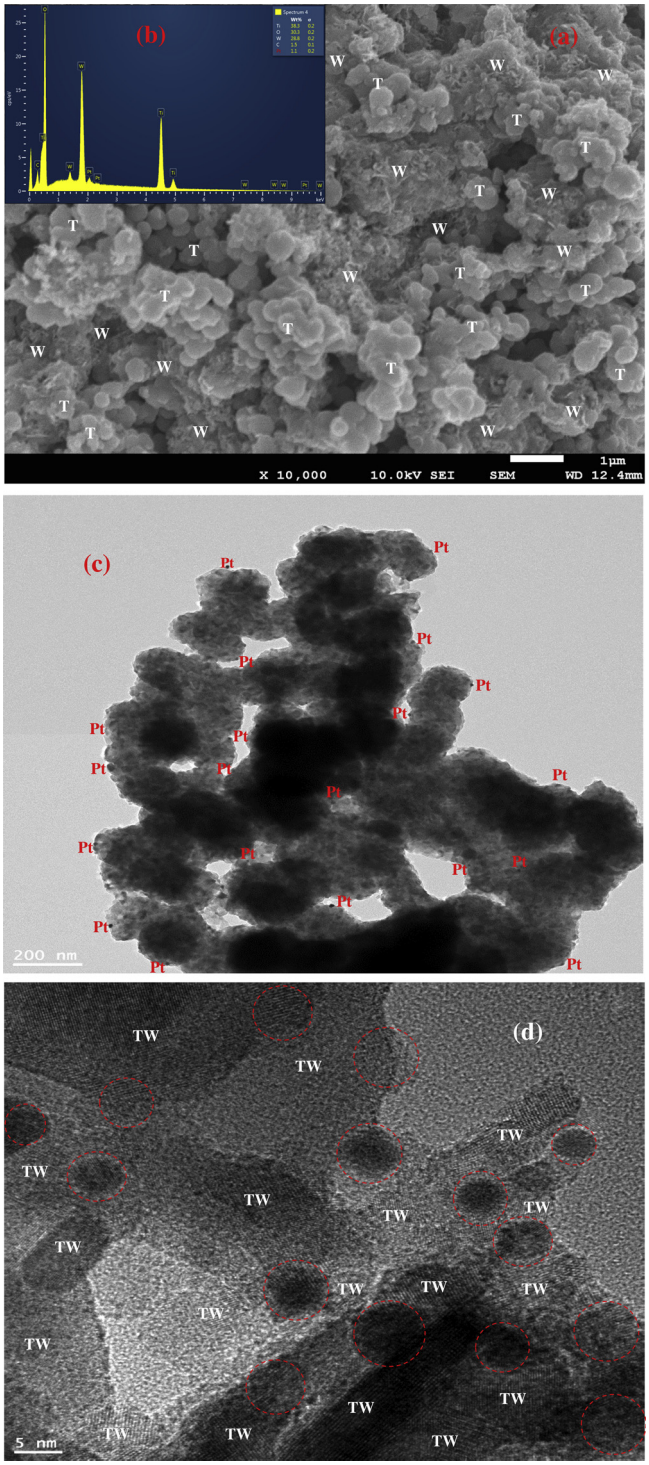

Fig. 2. Microscopy micrographs of calcined $Pt_{0.8}TW$ sample, (a) SEM image, (b) SEM-EDX spectra, (c) and (d) TEM images.

We recorded electron microscopy images of the samples. We report the images of $Pt_{0.8}TW$ sample as a representative (Fig. 2(a–d)). The SEM image (Fig. 2(a)) and the TEM images (Fig. 2(c–d)) clearly demonstrate the homogenous and uniform distribution of TiO_2 and WO_3 powders, besides the uniform deposition of Pt particles highlighted in red dotted circles. The SEM-EDX spectra (Fig. 2(b)) illustrates the presence of Pt, Ti and W elements. Moreover, the SEM micrographs show the micron size spherical TiO_2 particles and needle like morphology of WO_3 particles (Fig. S1, supplementary information). In summary the microscopy

images validate the very high interparticle connection network among TiO_2 and WO_3 particles with deposited Pt. Therefore, we may expect higher charge separation, electron storage and transfer among the particles.

N_2 adsorption and desorption measurement were performed to evaluate the texture of the powders. We measured the BET (Brunauer–Emmett–Teller) surface area and the BJH (Barrett–Joyner–Halenda) pore size distribution (percentage) and diameter) (Table 1). The pore diameter for the control $Pt_{0.8}W$ and $Pt_{0.8}T$ is 30 nm and 1.3 nm, respectively, and for the hybrid (Pt_xTW) samples ranges from 1.1 to 1.6 nm. The N_2 isotherms (Fig. S2, supplementary information) illustrates the overlapping type I(b) - type II isotherms, signifying the coexistence of micro, meso and macropores. Type I(b) (P/P_0 0.005-0.1) is associated with materials having broad micropore size distribution and narrow mesopores (< 2.5 nm) [31]. The measured diameter of such pores is between 1.1–1.6 nm (V-t method). The subsequent type II isotherms (P/P_0 0.1-0.995) reveals a meso-macroporous structure due to the lack of plateau at the maximum filling pressure, which is typical for spray dried nanoparticles suspensions [32]. The $Pt_{0.8}W$ sample is highly porous with low surface area (55 m^2/g) compared to $Pt_{0.8}T$ having high surface area (265 m^2/g). With the Pt deposition on composite samples the specific surface area is general lower, while staying above 200 m^2/g. The specific surface area increased until a maximum for the $Pt_{0.8}TW$ (283.0 m^2/g), and afterwards further decreased with an increase in the Pt amount. The samples surface area results are consistent with XRD crystallite size results and the SEM micrograph (Fig. 2(a) and Fig. S1 supplementary information) suggesting that the porosity relates to the voids between interrelated oxide particles. Moreover, all the synthesized samples are composed of micro, meso and macro pores. The observed nanoporous structures and large BET surface area are significant for photocatalysis, since they could be the source of transport channels for the molecules involved in the process redox reactions and effectively separate the photogenerated charge carriers, thus reducing the electron-hole pairs recombination [33,34].

We quantified the apparent band gap of the powders by adopting the Kubelka-Munk approximation [20] and building the Tauc plots $((\alpha h\upsilon)^{0.5}$ versus $h\upsilon)$ (Fig. 3). The apparent band gap values are listed in Table 1. The control $Pt_{0.8}W$ (2.3 eV) sample has a very narrow band gap compared to $Pt_{0.8}T$ (2.8 eV), highlighting that the deposited Pt is capable of harvesting visible light in WO_3 and TiO_2. The hybrid samples are also characterized by a greater red shift with an increase in Pt content up to 1.0 wt. %, indicating that the samples are prone to visible light absorption. In summary, in addition to WO_3, the deposited Pt on the photocatalyst surface is capable to significantly absorb the visible light [35]. The decrease in apparent band gap energy leads to rapid excitation of electrons from VB to CB in both the semiconductor oxides by absorbing of low photon energy, which increases the photocatalytic activity as well as the electron storage ability in WO_3 and in Pt particles

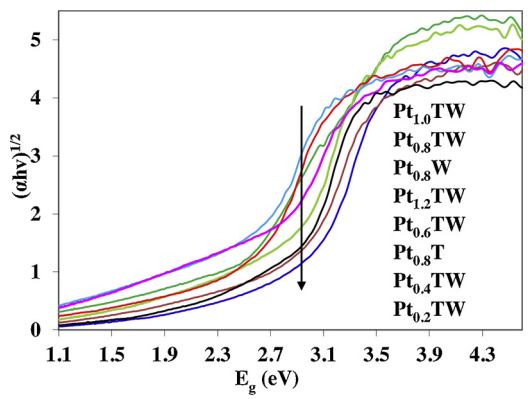

Fig. 3. Diffuse reflectance UV–vis- spectra.

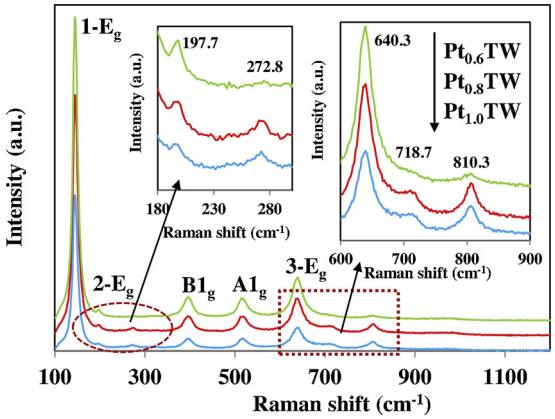

Fig. 4. Raman spectra (insert, magnified image of the pointed areas in the main spectra).

to exploit later in the absence of irradiation.

To further support the XRD data, we recorded Raman spectra (Fig. 4 and Fig. S3 (supplementary information)). In the hybrid powders, the peaks at 144.7 cm^{-1} (1-E_g) and 197.4 cm^{-1} (2-E_g) ascribe to the symmetric stretching vibration of oxygen atoms in O—Ti—O bond. 397.4 cm^{-1} (B_{1g}) and 516.7 cm^{-1} (A_{1g}) are caused by symmetric and anti symmetric bending vibration of O-Ti-O bond. 640.3 cm^{-1} (3-E_g) is the fifth most prominent peaks corresponding to anatase TiO_2 [36,37]. The typical features belonging to WO_3 monoclinic phase are the peaks observed at 272, 640.3, 718.7 and 810.3 cm^{-1} (highlighted in Fig. 4 insert), attributed to W—O—W bending vibration of bridging oxygen, stretching modes arising from W, H_2O and stretching of W—O—W bonds, respectively [38]. Moreover, all the Raman peaks are sharp and intense illustrating the well crystalline nature of the as-prepared powders.

The decrease in photogenerated electron-hole pairs recombination is one of the main prerequisite for enhanced photocatalytic activity. In the photoluminescence (PL) spectra of the selected powders there is a decrease in PL intensity following the trend $Pt_{0.8}W$ > $Pt_{0.4}TW$ > $Pt_{1.2}TW$ > $Pt_{0.8}T$ > $Pt_{0.6}TW$ > $Pt_{0.8}TW$. This indicates that $Pt_{0.8}TW$ sample has the lowest carrier recombination rate (Fig. 5). This further corroborates the synergistic effect of charge separation promoted by WO_3 together with the charge transfer promoted by Pt [1]. The Pt amount of 0.8 wt.% comes is the optimum amount to be deposited on the photocatalysts surface. A further increase in Pt (> 0.8 wt. %) may create surface defect sites that act as a recombination center for the charge carriers. Therefore, based on the PL analysis, the hybrid powders (in particular, $Pt_{0.6}TW$ and $Pt_{0.8}TW$) should be photocatalytically more active compared to control samples, because of the improved electron-hole separation and diffusion.

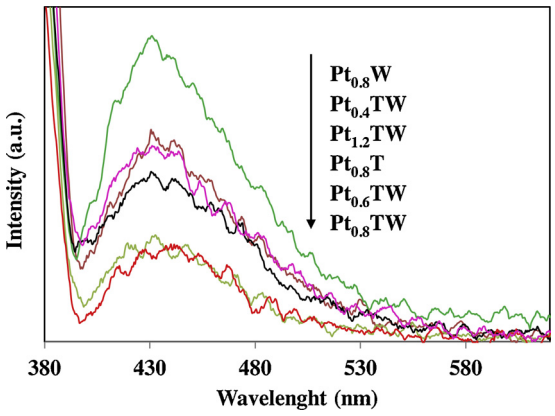

Fig. 5. Photoluminescence (PL) spectra.

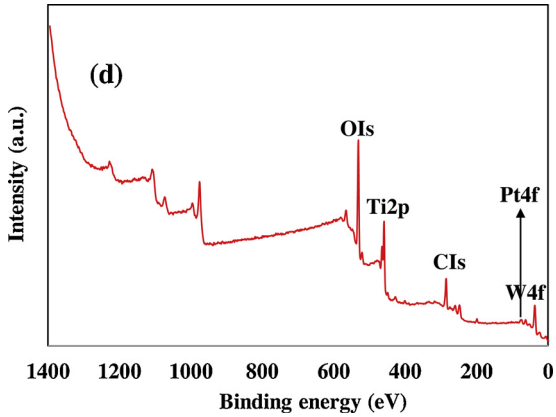

Fig. 6. XPS spectrum of $Pt_{0.8}W$ sample.

To investigate the oxidation state of the elements, we performed XPS (X-ray photoelectron spectroscopy) analysis on the representative $Pt_{0.8}TW$ sample. Fig. 6 represents the overview of the XPS spectrum relative to O, Ti, Pt and W and containing their corresponding photoelectron peaks O1s, Ti2p, Pt4f and W4f, respectively. The relative atomic percentage of the elements determined form the XPS data were about 68.4, 15.4, 12.0, 2.5 and 1.7 at. % for O, Ti, W, C, and Pt, respectively. The calibration of the all the peaks is referred to C1s, corresponding to the adventitious carbon from the XPS instrument.

The core level C1s peak (Fig. 7(a)) is composed of peaks at 285.0 eV and 286.1 eV, corresponding to C—C and C—O—C. The distinct shoulder at 389.2 eV corresponds to the surface carbonate species or to O—C═O/C═O, typical of carbon adsorbed on the sample [39]. The high resolution O1s spectrum (Fig. 7(b)) can be easily fitted to three peaks: 530.6 eV represents lattice oxygen bound to Ti^{4+}/W^{6+}, while the other two peaks result form the influence of absorbed water on the surface. 531.9 eV corresponds to surface hydroxyl groups with oxygen at the bridging oxygen site (OH_{br}), and 532.9 eV originate from the OH group as a terminal group (OH_t) with oxygen attached to Ti^{4+}/W^{6+} (W—O—Ti) [40]. In the Ti2p spectrum (Fig. 7(c), the peaks at binding energy of 459.05 eV and 464.7 eV correspond to Ti^{4+}. The spectrum of Pt4f peak (Fig. 7(d)) can be divided into the two peaks of $Pt4f_{7/2}$ (70.9 eV) and $Pt4f_{5/2}$ (74.1 eV), indicating the presence of metallic Pt (Pt°) [41]. The deconvoluted peak of W4f in Fig. 7(e) with binding energy of 35.6 eV ($W4f_{7/2}$) and 37.7 eV ($W4f_{5/2}$) ascribed to W^{6+} oxidation state [25]. The corresponding spin-orbital separation in the W4f doublet is 2.1 eV, which agrees with the theoretical value for WO_3. In summary, in agreement with the FTIR data, surface OH^- groups and adsorbed water are beneficial to assist photocatalyst activity. Also, in compliance with the microscopy and Raman data, the oxygen linkages with Ti and W demonstrates a network connection between the two semiconductors, which promotes the charge separation. Moreover, XPS detected the presence of metallic Pt (Pt°), which is the oxidation state in which Pt is most photocatalytically active [39]. Pt also acts as a storage center for the photogenerated electrons to exploit later on in the redox processes in the absence of light. Thus, we expect the hybrid powder to be active both under light irradiation, as well as in the dark.

3.2. Photocatalytic activity

To evaluate the UV–vis photocatalytic activity of the prepared samples, we performed the degradation of the model pollutant methylene blue (MB) in water. Blank experiments (photolysis, 30 min) were performed by irradiating (UV and visible light) the aqueous solution of the model pollutant in the absence of photocatalyst under identical conditions (Fig. 8(a–b)): the concentration of MB did not change [42,43], which confirms that a catalyst is necessary to cleave the molecule of the model pollutant. The dark adsorption equilibrium of

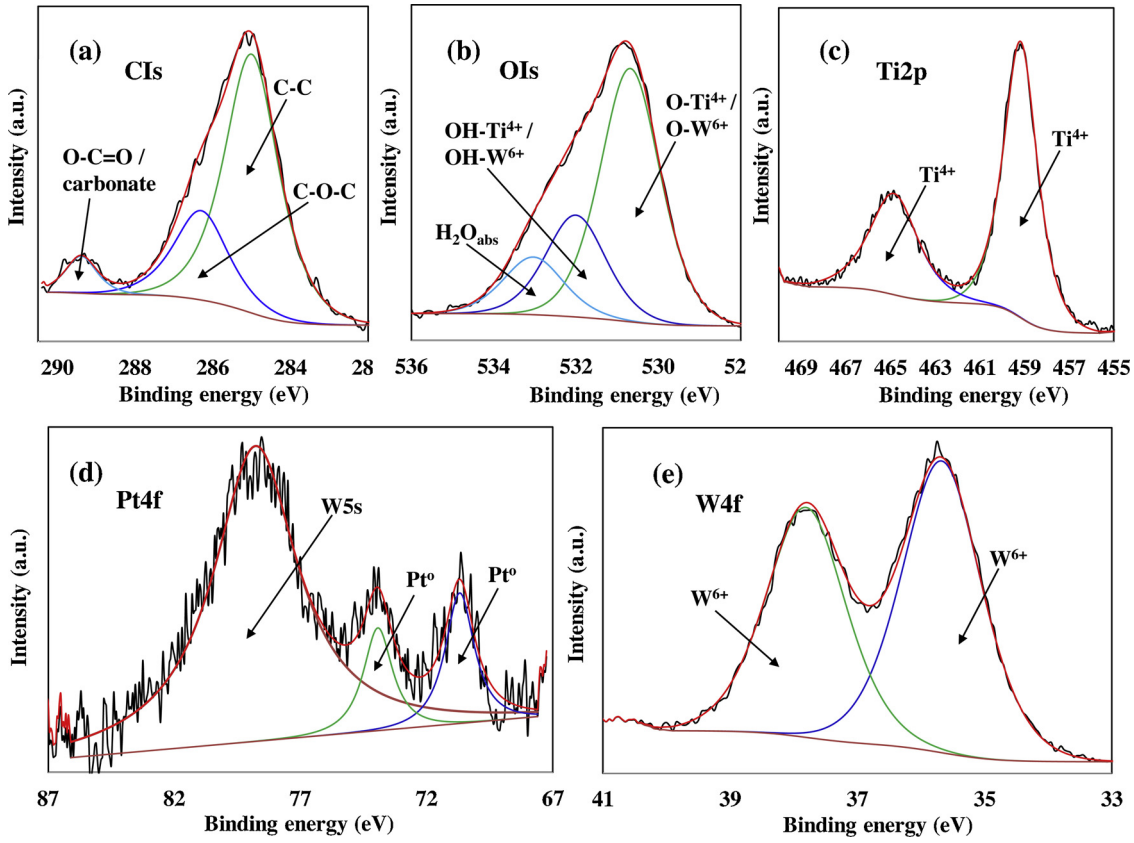

Fig. 7. High resolution spectra of (a) C1s, (b) O1s, (c) Ti2p, (d) Pt4f, (i) W4f of $Pt_{0.8}W$ sample.

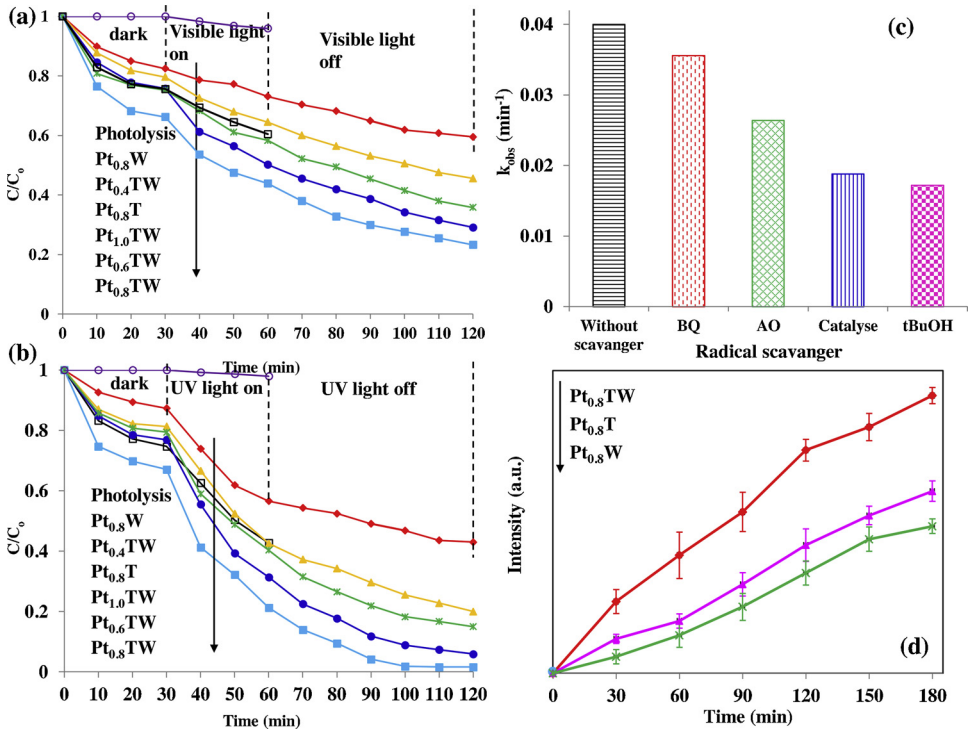

Fig. 8. Photolysis and photocatalytic tests of the samples calcined at 600 °C under (a) UV and (b) Vis light irradiation against methylene blue (MB) degradation, (c) observed reaction rate constants (k_{obs}) for the degradation of MB by $Pt_{0.8}TW$ with and without different scavengers and (d) change in photoluminescence (PL) intensity of the dispersed TA solution under UV illumination for the selected calcined samples. We report standard deviation (< 1%) in the supplementary information.

the MB molecules on the photocatalyst surface occurred around 30 min. Relative adsorption of the pollutant molecules on the photocatalyst powder surface are illustrated in Table S1 (supplementary information). The hybrid samples ($Pt_{0.8}TW$) are characterized by both higher dark MB adsorption and UV-vis activity compared to other samples (Fig. 8(a–b) and Fig. S4 (supplementary information)). In the UV experiments, $Pt_{0.8}TW$ degrade ≈ 98% MB compared to the control sample $Pt_{0.8}W$ (66% MB) in 120 min (30 min dark + 30 min light + 60 min dark), while the control $Pt_{0.8}T$ degraded 57% MB in 60 min (30 min dark + 30 min light). It is well understood that the $Pt_{0.8}T$ has no electron storage ability. Similar activity trend was observed in the visible experiments $Pt_{0.8}TW > Pt_{0.6}TW > Pt_{1.0}TW \approx Pt_{0.8}T$ (60 min) > $Pt_{0.4}TW > Pt_{0.8}W$, stating that the $Pt_{0.8}TW$ sample degrade ≈ 77% MB in 120 min. The higher photocatalytic activity of $Pt_{0.8}TW$ against the MB molecules may be connected to its high BET surface area along with its porous structure, higher concentration of surface OH^- groups and adsorbed water, lower band gap and carrier recombination due to the synergistic effect of coupling the semiconductors and homogeneous Pt dispersion (distributed electron transfer). The high surface area adsorbs more pollutant, while the macro-meso-microporous structure promotes the diffusion of the pollutant molecules inside and outside the catalysts particles. Surface adsorbed water and OH^- groups generates a greater surface $OH^•$ radicals concentration reacting with the photopromoted holes. The electron-holes separation and their diffusion to the active sites to take part in the redox reactions is the key factor for photocatalytic activity. Coupling TiO_2 and WO_3 promotes the diffusion of electrons and holes between the different oxide energy bands (CB and VB), thus decreasing the recombination rate. Also, due to the presence of Pt, a further decrease in this recombination occurs as result of the Schottky barrier formed at the interface of the metal (Pt) and the semiconductor oxides [25,44]. The excited CB electrons are then channeled from the bulk of WO_3/TiO_2 to the newly formed interface and, as consequence, the electron density in the oxides particles will decrease, thus preventing energy waste and increasing the photocatalytic activity.

The $Pt_{0.8}W$ and the hybrid samples (Pt_xTW) were still active in absence of irradiation. The highly active sample $Pt_{0.8}TW$ degraded an extra 20% and 21% MB compared to $Pt_{0.8}W$ sample, which degraded 13% and 14% after the UV and visible lights were switched off, respectively. (Fig. 8(a–b)). The energy storage trend in the samples was $Pt_{0.8}TW > Pt_{0.6}TW > Pt_{1.0}TW > Pt_{0.4}TW > Pt_{0.8}W$. We explain the photoactivity and energy storage capacity trend in the following section with a proposed mechanism.

3.3. Role of radical scavenger and photocatalyst stability

Reactive oxidizing species (ROS) such as super oxide anions ($O_2^{-•}$), hydroxyl radicals ($OH^•$), hydrogen peroxides (H_2O_2), besides the photogenerated holes, are the main active molecules responsible for the degradation of pollutants in any photocatalytic process. To probe the observed trend among the possible ROS responsible for higher activity, we conducted experiments in the presence of several sacrificial agents including 1,4 benzoquinone (BQ, superoxide anions quencher ($O_2^{-•}$)), catalase (catalyses the dismutation of H_2O_2), ammonium oxalate (AO, scavenge photogenerated hole (h^+)) and tert-butanol (tBuOH, scavenge hydroxyl radicals) [45,46], following the same procedure stated in our published work [20]. At our experimental conditions, the UV observed photodegradation rate (k_{obs}) of MB in the presence of the most active sample ($Pt_{0.8}TW$) decreased by 11, 34, 53 and 57% with BQ, AO, CAT, and *t*BuOH as sacrificial agents, respectively (Fig. 4(c)). We can therefore conclude that primarily H_2O_2, $OH^•$ followed by $O_2^{-•}$ and h^+ are responsible for the decomposition of the pollutant MB. To further ascertain the involvement of the active $OH^•$ radicals, the intensity of the highly fluorescent 2-hydroxy terephthalic acid (TAOH) was measured versus UV irradiation time. TAOH produces from the reaction between terephthalic acid (TA) and $OH^•$ radicals. Fig. 8(d) illustrates that the hybrid sample $Pt_{0.8}TW$ produces a larger amount of $OH^•$ radicals compared to the control samples ($Pt_{0.8}T$ and $Pt_{0.8}W$), which agree with the FTIR analysis exhibiting adsorbed H_2O peak and the very broad trough for the surface OH- groups for $Pt_{0.8}TW$. In addition, the narrower band gap of $Pt_{0.8}TW$ is responsible for more UV light absorption, thus producing more h^+ species, which are main scavenging agents for the OH- groups to generate $OH^•$ radicals.

Inductively coupled plasma–mass spectrometry (ICP–MS) assessed the stability of the Pt_xT powders. ICP is generally used to quantify trace metallic and non-metallic elements in solution [47]. Therefore, at the

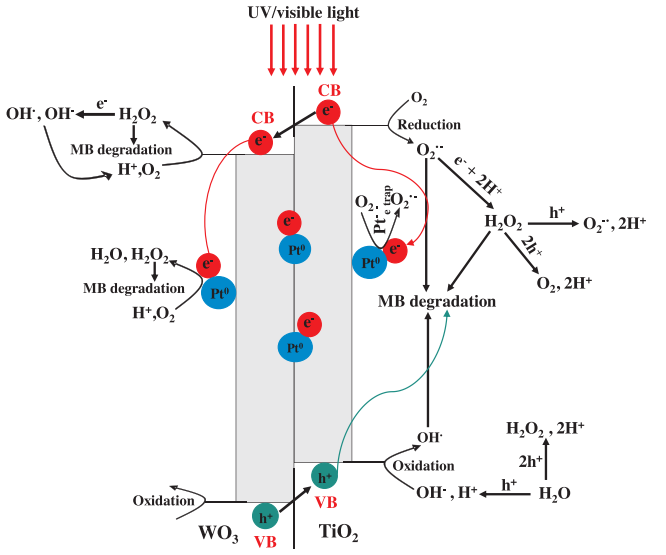

Fig. 9. Proposed mechanism illustrating the transfer pathways of the photo-promoted electrons and holes and various oxidizing species contributing to the degradation of methylene blue (MB).

end of each UV photocatalytic activity experiment, the ICP–MS analyzed an aliquot to estimate the Pt, W and Ti content. The atomic percentages of Pt, W and Ti are shown in the supplementary information (Table S2), indicating that all samples except $Pt_{1.0}TW$ retain Pt better than the control samples possibly because of the large Pt_x-TW interface through the high surface area. This induced a strong interaction to anchor Pt tightly on the oxides surface (Fig. 9).

3.4. Proposed mechanism

In the hybrid samples (Pt_xTW), under UV–vis irradiation electrons are excited from the valance bands (VB) to the conduction bands (CB) of the semiconductor oxides (TiO_2/WO_3), while leaving holes in the VBs (Fig. 6). The externally supplied oxygen in the presence of CB electrons is converted into superoxide anions ($O_2^{-\bullet}$) on the catalyst surface, which further generate hydrogen peroxide (H_2O_2) [11] through successive reactions. The VB holes (h^+) are scavenged by adsorbed H_2O to produces H_2O_2 ($2H_2O + 2h^+ \rightarrow 2H^+ + H_2O_2$) [48], or generate hydroxyl groups (OH-), which on further reaction with the VB holes yield the highly reactive hydroxyl ($OH^\bullet$) radicals. The produced oxidizing species (H_2O_2, $OH^\bullet$), in addition to $O_2^{-\bullet}$ and the photogenerated h^+ then take part in the decomposition of the pollutant (MB) molecules. In our ROS experiments, we observed that H_2O_2 and $OH^\bullet$ are the major photocatalytic species. Indeed, this may be due to the difference in the CB and VB energy level of the oxides, which causes a substantial migration of electrons from the CB of TiO_2 to the one of WO_3, and of holes from the VB of WO_3 to the one of TiO_2. As a result, the electrons in the CB of WO_3 are efficiently exploited in the production of H_2O_2, as discussed earlier. The H_2O_2 has also the ability to react either with CB electrons to generate $OH^\bullet$ and OH- species or with VB holes to produce superoxide anions ($O_2^{-\bullet}$) or oxygen (O_2), thus preventing electron hole recombination [48].

The H_2O_2 production, electron storage ability and electron-hole separation can be further enhanced on the deposition of Pt on the semiconductor oxides. In support of XPS and UV–vis-DRS analysis, the loaded metallic Pt on WO_3 and TiO_2 mainly function as a co-catalyst to enhance visible light absorption and the photocatalytic performance of the hybrid samples. Through a lower over-potential it provides the multielectron reduction pathways for oxygen. The loaded Pt° particles can act as an electron sink to capture, store and release electrons diffused from the excited semiconductors to produce superoxide anions, in addition to the increase in the electrons-holes separation. In the dark, the electrons captured by the metallic Pt or stored in the WO_3 CB band are discharged (e.g., $O_2 + 2H^+ + 2e^- \rightarrow H_2O_2(aq)$; $4H^+ + O_2 + 4e^- \rightarrow 2H_2O\,(aq)$, $H_2O_2 + e^- \rightarrow OH^- + OH^\bullet(aq)$) and they react just as the photoelectrons do, thus facilitating the MB pollutant oxidation, exhibiting MB degradation in the dark [24]. In summary, the samples reported in the present work are more active and have greater energy storage ability than the samples in pure previous work [20]. Indeed, they maintained the activity under both UV and Vis irradiation for an extra 80 min. The Pt_xTW sample degraded 75% and almost 100% MB in the presence of UV and Vis irradiation in 120 min, respectively, being the last 80 min in the dark

4. Conclusions

We described a facile, scalable synthesis through spray drying of highly active Pt/TiO_2-WO_3 materials under both UV and Vis irradiation. We varied the amount of Pt from 0.2 to 1 wt.%. The optimum amount was 0.8 wt.% and Pt was homogeneously dispersed. This powder had the highest surface area (283 $m^2\ g^{-1}$) and the highest % of macro-meso pores among the hybrid samples. It also had the lowest electron-hole recombination rate (photoluminescence measurements) and the highest amount surface hydroxyl groups (FTIR). After 40 min of activity under either UV or Vis light, our samples had an energy storage ability with residual activity in the dark for 80 min. The Pt_xTW sample degraded 75% and almost 100% MB in the presence of visible and UV irradiation in 120 min, respectively, being the last 80 min in the dark. The high activity of the samples ascribes to the synergistic effect of both WO_3 and Pt as co-catalyst for TiO_2. This synergistic effect includes the charge separation promoted by WO_3 together with the charge transfer promoted by Pt. Furthermore, the prepared samples were stable demonstrating good anchoring of Pt particles on the oxides surface, opening up the possibility of adopting these hybrid materials in the UV–vis photo-oxidation processes to remove toxic and hazardous aqueous pollutants.

Conflict of interest

The authors declare that there is no conflict of interests regarding the publication of this paper.

Acknowledgements

The authors gratefully acknowledge the Fonds de Recherche du Québec – Nature et technologies (FRQNT) to provide support for this research. Special thanks go to Dr. C. Daniel (Department of Chemistry, University of Montreal), Prof. Sasha Omanovic (Dept. of Chemical Engineering, McGill University), Department of Chemistry and Department of Chemical Engineering, McGill University to allow the use of their laboratory analytical instruments such as the PL, ICP-MS, UV–vis DRS, FTIR for the photocatalyst characterization and activity tests.

The authors gratefully acknowledge the support of the Natural Sciences and Engineering Research Council of Canada (NSERC). This research was undertaken, in part, thanks to funding from the Canada Research Chairs program.

Appendix A. Supplementary data

Supplementary material related to this article can be found, in the online version, at doi:https://doi.org/10.1016/j.apcatb.2019.04.019.

References

[1] D. Spanu, S. Recchia, S. Mohajernia, P. Schmuki, M. Altomare, Site-selective Pt dewetting on WO_3-coated TiO_2 nanotube arrays: an electron transfer cascade-based

H_2 evolution photocatalyst, Appl. Catal. B: Environ. 237 (2018) 198–205.
[2] W.A. Saoud, A.A. Assadi, M. Guiza, S. Loganathan, A. Bouzaza, W. Aboussaoud, A. Ouederni, S. Rtimi, D. Wolbert, Synergism between non-thermal plasma and photocatalysis: implicationsin the post discharge of ozone at a pilot scale in a catalytic fixed-bed reactor, Appl. Catal. B: Environ. 241 (2019) 227–235.
[3] M. Stucchi, F. Galli, C.L. Bianchi, C. Pirola, D.C. Boffito, F. Biasioli, V. Capucci, Simultaneous photodegradation of VOC mixture by TiO_2 powders, Chemosphere 193 (2018) 198–206.
[4] M. Stucchi, C.L. Bianchi, C. Argirusis, V. Pifferi, B. Neppolian, G. Cerrato, D.C. Boffito, Ultrasound assisted synthesis of Ag-decorated TiO_2 active in visible light, Ultrason. Sonochem. 40 (2018) 282–288.
[5] M.V. Dozzi, S. Marzorati, M. Longhi, M. Coduri, L. Artiglia, E. Selli, Photocatalytic activity of TiO_2-WO_3 mixed oxides in relation to electron transfer efficiency, Appl. Catal. B: Environ. 186 (2016) 157–165.
[6] C. Pirola, D.C. Boffito, S. Vitali, C.L. Bianchi, Photocatalytic coatings for building industry: study of 1 year of activity in the NO_x degradation, J. Coat. Technol. Res. 9 (2012) 453–458.
[7] G. Cerrato, C.L. Bianchi, F. Galli, C. Pirola, S. Morandi, V. Capucci, Micro-TiO_2 coated glass surfaces safely abate drugs in surface water, J. Hazard. Mater. 363 (2019) 328–334.
[8] C.L. Bianchi, C. Pirola, F. Galli, S. Vitali, A. Minguzzi, M. Stucchi, F. Manenti, V. Capucci, NO_x degradation in a continuous large-scale reactor using full-size industrial photocatalytic tiles, Catal. Sci. Technol. 6 (2016) 2261–2267.
[9] D.C. Boffito, V. Crocella, C. Pirola, B. Neppolian, G. Cerrato, M. Ashokkumar, C.L. Bianchi, Ultrasonic enhancement of the acidity, surface area and free fatty acids esterification catalytic activity of sulphated ZrO_2–TiO_2 systems, J. Catal. 297 (2013) 17–26.
[10] M. Stucchi, C.D. Boffito, E. Pargoletti, G. Cerrato, L.C. Bianchi, G. Cappelletti, Nano-MnO_2 decoration of TiO_2 microparticles to promote gaseous ethanol visible photoremoval, Nanomaterials 8 (2018) 1–12.
[11] N.A. Ramos-Delgado, L. Hinojosa-Reyes, I.L. Guzman-Mar, M.A. Gracia-Pinilla, A. Hernandez-Ramirez, Synthesis by sol–gel of WO_3/TiO_2 for solar photocatalytic degradation of malathion pesticide, Catal. Today 209 (2013) 35–40.
[12] A.K.L. Sajjad, S. Shamaila, B. Tian, F. Chen, J. Zhang, Comparative studies of operational parameters of degradation of azo dyes in visible light by highly efficient WO_x/TiO_2 photocatalyst, J. Hazard. Mater. 177 (2010) 781–791.
[13] H. Zheng, J.Z. Ou, M.S. Strano, R.B. Kaner, A. Mitchell, K. Kalantar-Zadeh, Nanostructured tungsten oxide – properties, synthesis, and applications, Adv. Funct. Mater. 21 (2011) 2175–2196.
[14] G. Zerjav, M.S. Arshad, P. Djinovic, J. Zavasnik, Pintar, A.; Electron trapping energy states of TiO_2–WO_3 composites and their influence on photocatalytic degradation of bisphenol A, Appl. Catal. B: Environ. 209 (2017) 273–284.
[15] F. Riboni, L.G. Bettini, D.W. Bahnemann, E. Selli, WO_3–TiO_2 vs. TiO_2 photocatalysts: effect of the W precursor and amount on the photocatalytic activity of mixed oxides, Catal. Today 209 (2013) 28–34.
[16] L. Baia, E. Orban, S. Fodor, B. Hampel, E.Z. Kedves, K. Saszet, I. Szekely, E. Karacsonyi, B. Reti, P. Berki, A. Vulpoi, K. Magyari, A. Csavdari, C. Bolla, V. Cosoveanu, K. Hernadi, M. Baia, A. Dombi, V. Danciu, G. Kovacs, Z. Pap, Preparation of TiO_2/WO_3 composite photocatalysts by the adjustment of the semiconductors' surface charge, Mater. Sci. Semicond. Process. 42 (2016) 66–71.
[17] P. Pandi, C. Gopinathan, Synthesis and characterization of TiO_2–NiO and TiO_2–WO_3 nanocomposites, J. Mater. Sci.: Mater. Electron. 28 (2017) 5222–5234.
[18] K.K. Akurati, A. Vital, J.P. Dellemann, K. Michalow, T. Graule, D. Ferri, A. Baiker, Flame-made WO_3/TiO_2 nanoparticles: relation between surface acidity, structure and photocatalytic activity, Appl. Catal. B: Environ. 79 (2008) 53–62.
[19] L. Cao, J. Yuan, M. Chen, W. Shangguan, Photocatalytic energy storage ability of TiO_2-WO_3 composite prepared by wet-chemical technique, J. Environ. Sci. 22 (2010) 454–459.
[20] H. Khan, M.G. Rigamonti, G.S. Patience, D.C. Boffito, Spray dried TiO_2/WO_3 heterostructure for photocatalytic applications with residual activity in the dark, Appl. Catal. B: Environ. 226 (2018) 311–323.
[21] M. Tasbihi, F. Fresno, U. Simon, I.J. Villar-Garcia, V. Perez-Dieste, C. Escudero, V.A. de la Pena Oshea, On the selectivity of CO_2 photoreduction towards CH_4 using Pt/TiO_2 catalysts supported on mesoporous silica, Appl. Catal. B: Environ. 239 (2018) 68–76.
[22] E. Antolini, Photo-assisted methanol oxidation on Pt-TiO_2 catalysts for direct methanol fuel cells: a short review, Appl. Catal. B: Environ. 237 (2018) 491–503.
[23] W.H. Saputera, J.A. Scott, D. Friedmann, R. Amal, Revealing the key oxidative species generated by Pt-loaded metal oxides under dark and light conditions, Appl. Catal. B: Environ. 223 (2018) 216–227.
[24] R. Abe, H. Takami, N. Murakami, B. Ohtani, Pristine simple oxides as visible light driven photocatalysts: highly efficient decomposition of organic compounds over platinum-loaded tungsten oxide, J. Am. Chem. Soc. 130 (2008) 7780–7781.
[25] M. Qamar, Z.H. Yamani, M.A. Gondal, K. Alhooshani, Synthesis and comparative photocatalytic activity of Pt/WO_3 and Au/WO_3 nanocomposites under sunlight-type excitation, Sol. State Sci. 13 (2011) 1748–1754.
[26] T. Ohashi, T. Sugimoto, K. Sako, S. Hayakawa, K. Katagiri, K. Inumaru, Enhanced photocatalytic activity of Pt/WO_3 photocatalyst combined with TiO_2 nanoparticles by polyelectrolyte-mediated electrostatic adsorption, Catal. Sci. Technol. 5 (2015) 1163–1168.
[27] H. Khan, Sol–gel synthesis of TiO_2 from $TiOSO_4$: characterization and UV photocatalytic activity for the degradation of 4-chlorophenol, React. Kinet. Mech. Cat. 121 (2017) 811–832.
[28] D. Nasuhoglu, V. Yargeau, D. Berk, Photo-removal of sulfamethoxazole (SMX) by photolytic and photocatalytic processes in a batch reactor under UV-C radiation (λ_{max} = 254 nm), J. Hazar. Mater. 186 (2011) 67–75.
[29] N.T. Nolan, M.K. Seery, S.C. Pillai, Spectroscopic investigation of the anatase-to-rutile transformation of sol – gel-synthesized TiO_2 photocatalysts, J. Phy. Chem. C. 113 (2009) 16151–16157.
[30] J. Diaz–Reyes, V. Dorantes–Garcia, A. Perez–Benitez, J.A. Balderas–Lopez, Obtaining of films of tungsten trioxide (WO_3) by resistive heating of a tungsten filament, Superficies y Vacio 21 (2008) 12–17.
[31] M. Thommes, K. Kaneko, A.V. Neimark, J.P. Olivier, F.R. Reinoso, J. Rouquerol, S.W.S. Kenneth, Physisorption of gases, with special reference to the evaluation of surface area and pore size distribution (IUPAC Technical Report), Pure Appl. Chem. (2015) 1051–1069.
[32] M.G. Rigamonti, Y.X. Song, H. Li, N. Saadatkhah, P. Sauriol, G.S. Patience, Influence of atomization conditions on spray drying lithium iron phosphate nanoparticle suspensions, Can. J. Chem. Eng. (2018) 1–9.
[33] H. Song, Y. Li, Z. Lou, M. Xiao, L. Hu, Z. Ye, L. Zhu, Synthesis of Fe-doped WO_3 nanostructures with high visible-light-driven photocatalytic activities, Appl. Catal. B: Environ. 166-167 (2015) 112–120.
[34] M. Stucchi, A. Elfiad, M. Rigamonti, H. Khan, D.C. Boffito, Water treatment: Mn-TiO_2 synthesized by ultrasound with increased aromatics adsorption, Ultrason. Sonochem. 44 (2018) 272–279.
[35] F.B. Li, X.Z. Li, The enhancement of photodegradation efficiency using Pt–TiO_2 catalyst, Chemosphere 48 (2002) 1103–1111.
[36] H.C. Choi, Y.M. Jung, S.B. Kim, Size effects in the Raman spectra of TiO_2 nanoparticles, Vib. Spectrosc. 37 (2005) 33–38.
[37] B. Prajapati, S. Kumar, M. Kumar, S. Chatterjee, A.K. Ghosh, Investigation of the physical properties of Fe:TiO_2-diluted magnetic semiconductor nanoparticles, J. Mater. Chem. C. 5 (2017) 4257–4267.
[38] S. Bai, K. Zhang, L. Wang, J. Sun, R. Luo, D. Li, A. Chen, Synthesis mechanism and gas-sensing application of nanosheet-assembled tungsten oxide microspheres, J. Mater. Chem. A 2 (2014) 7927–7934.
[39] K. Siuzdak, M. Sawczak, M. Klein, G. Nowaczyk, S. Jurga, A. Cenian, Preparation of platinum modified titanium dioxide nanoparticles with the use of laser ablation in water, Phys. Chem. Chem. Phys. 16 (2014) 15199–15206.
[40] P. Krishnan, M. Liu, P.A. Itty, Z. Liu, V. Rheinheimer, M.H. Zhang, P.J.M. Monteiro, L.E. Yu, Characterization of photocatalytic TiO_2 powder under varied environments using near ambient pressure X-ray photoelectron spectroscopy, Sci. Rep. 7 (2017) 43298–43309.
[41] Y.H. Li, J. Xing, Z.J. Chen, Z. Li, F. Tian, L.R. Zheng, H.W. Feng, P. Hu, H.Z. Jun, H.Y. Gui, Unidirectional suppression of hydrogen oxidation on oxidized platinum clusters, Nat. Commun. 4 (2013) 2500–2507.
[42] T. Soltani, M.H. Entezari, Photolysis and photocatalysis of methylene blue by ferrite bismuth nanoparticles under sunlight irradiation, J. Mol. Catal. A: Chem. 377 (2013) 197–203.
[43] F. Azeez, E. Al-Hetlani, M. Arafa, Y. Abdelmonem, A.B. Nazeer, M.O. Amin, M. Madkour, The effect of surface charge on photocatalytic degradation of methylene blue dye using chargeable titania nanoparticles, Sci. Rep. 8 (2018) 7104–7113.
[44] Y. Ma, X. Wang, Y. Jia, X. Chen, H. Han, C. Li, Titanium dioxide-based nanomaterials for photocatalytic fuel generations, Chem. Rev. 114 (2014) 9987–10043.
[45] N. Zhang, S. Liu, X. Fu, Y.J. Xu, Synthesis of M@TiO_2 (M = Au, Pd, Pt) core–shell nanocomposites with tunable photoreactivity, J. Phys. Chem. C 115 (2011) 9136–9145.
[46] M. Kamagate, A.A. Assadi, T. Kone, L. Coulibaly, K. Hanna, Activation of persulfate by irradiated laterite for removal of fluoroquinolones in multi-component systems, J. Hazard. Mater. 346 (2018) 159–166.
[47] M. Kamagate, A.A. Assadi, T. Kone, S. Giraudet, L. Coulibaly, K. Hanna, Use of laterite as a sustainable catalyst for removal of fluoroquinolone antibiotics from contaminated water, Chemosphere 195 (2018) 847–853.
[48] Y. Kakuma, A.Y. Nosaka, Y. Nosaka, Difference in TiO_2 photocatalytic mechanism between rutile and anatase studied by the detection of active oxygen and surface species in water, Phys. Chem. Chem. Phys. 17 (2015) 18691–18698.